nature materials

ARTICLES

https://doi.org/10.1038/s41563-021-01181-2

Check for updates

Photo-enhanced ionic conductivity across grain boundaries in polycrystalline ceramics

Thomas Defferriere[1,5]✉, Dino Klotz[1,2,5]✉, Juan Carlos Gonzalez-Rosillo[1,3], Jennifer L. M. Rupp[1,4] and Harry L. Tuller[1,2]✉

Grain boundary conductivity limitations are ubiquitous in material science. We show that illumination with above-bandgap light can decrease the grain boundary resistance in solid ionic conductors. Specifically, we demonstrate the increase of the grain boundary conductance of a 3 mol% Gd-doped ceria thin film by a factor of approximately 3.5 at 250 °C and the reduction of its activation energy from 1.12 to 0.68 eV under illumination, while light-induced heating and electronic conductivity could be excluded as potential sources for the observed opto-ionic effect. The presented model predicts that photo-generated electrons decrease the potential barrier heights associated with space charge zones depleted in charge carriers between adjacent grains. The discovered opto-ionic effect could pave the way for the development of new electrochemical storage and conversion technologies operating at lower temperatures and/or higher efficiencies and could be further used for fast and contactless control or diagnosis of ionic conduction in polycrystalline solids.

Fast ion conductors are essential components of solid-state electrochemical energy conversion, storage and sensor systems. This can be either as electrolytes in which conduction is solely by ions (that is, electronically insulating)[1–6] or in mixed ionic–electronic conductors of interest as solid-state battery electrodes[7–9], fuel cell electrodes[10–13] or gas permeation membranes[14]. The choice of solid-state conductor depends on the mobile ions of interest, ranging, for example, from oxygen and proton ion conductors such as $Ce_{1-x}Gd_xO_2$ (GDC), $Zr_{1-x}Y_xO_2$ and $BaZr_{1-x}Y_xO_3$, used in solid oxide fuel cells and electrolysers[1,3,12,15], to lithium and sodium conductors, such as $Li(Al,Ti)_2(PO_4)_3$, $Li_7La_3Zr_2O_{12}$, $Na_3Zr_2Si_2PO_{12}$ and Na-conducting β-alumina, used in solid-state batteries[16,17]. Though the mobile ions in the respective lattices have different charges and ionic radii, the governing transport dynamics of ion hopping are similar. In their most basic and cost-effective format, solid electrolytes are processed as ceramic pellets or plates via powder synthesis and densification by sintering, leading to a polycrystalline microstructure composed of grains and grain boundaries[18]. Grain boundaries are regions of higher defect density and disorder that tend to block the flow of ions between grains. Depending on grain boundary tilt angles, segregated impurities and dopants, and choice of processing routes (including choice of substrates for films), grain boundaries can lead to orders of magnitude decrease in effective ionic conductivity. For example, proton conductivity in $BaZr_{1-x}Y_xO_3$ with $x=0.05$ is depressed by nearly three orders of magnitude at 300 °C (refs. [19,20]) due to grain boundary blocking compared to its bulk conductivity. Measurements on GDC, particularly for lower dopant levels, have shown similar decreases in conductivity[21,22]. Likewise, measurements of Li conductivity in the perovskite $Li_{3x}La_{(2/3)-x}TiO_3$ (LLTO, $0<x<0.16$) have shown grain boundary conductivities to be as much as four orders of magnitude lower than the bulk conductivity[23–27]. The trend towards lower operating temperatures further amplifies this problem, as the grain boundary activation energies are typically higher than those of the bulk, thus dominating the low-temperature ionic transport behaviour even more.

A detailed review of the space charge nature of such barriers and how illumination is expected to modulate barrier height magnitudes and thereby grain boundary resistivity is presented in Supplementary Section 1. While these considerations are based on GDC, they apply also to other polycrystalline ionic conductors.

The impact of light on grain boundaries has been studied for polycrystalline silicon, demonstrating reduced grain boundary resistance when operated as a photodetector or solar cell under high optical illumination[28]. In this work we focus on the potential impact of illumination on the effective potential barrier experienced by ions, for which there is currently no referenced literature, to the best of our knowledge.

We have selected GDC as a model material, one of the most highly conducting oxygen ion solid electrolytes[29,30]. This was done, in part, because grain boundary blocking of ion transport in this system has been well characterized and confirmed to be dominated by the space charge depletion of oxygen vacancies[21,31] and because its bandgap energy of ~3 eV enables photo-generation of electron–hole pairs by readily accessible light sources (375 nm near-UV light-emitting diode (LED)). Because of their relatively larger grain boundary resistance contributions, we chose a lower dopant level (3 mol% Gd, in the following referred to as 3GDC) than what is typically selected to achieve maximum oxygen ion conductivity (10–20 mol% Gd)[31].

We use electrochemical impedance spectroscopy (EIS) to measure and deconvolute grain and grain boundary resistance contributions, both in the dark and under illumination. While deconvoluting grain and grain boundary contributions in polycrystalline thin films requires an advanced sample design[32,33], the epitaxial sample allows us to rule out possible effects of illumination within the bulk or at the surface of 3GDC playing a major role in increasing the conductivity of the polycrystalline sample. Furthermore, we use

[1]Department of Material Science and Engineering, MIT, Cambridge, MA, USA. [2]International Institute for Carbon-Neutral Energy Research (I2CNER), Kyushu University, Fukuoka, Japan. [3]Present address: Catalonia Institute for Energy Research, Universitat de Barcelona, Sant Adrià del Besòs, Spain. [4]Present address: Department of Chemistry, Technical University of Munich, München, Germany. [5]These authors contributed equally: Thomas Defferriere, Dino Klotz. ✉e-mail: tdefferr@mit.edu; dino.klotz@i2cner.kyushu-u.ac.jp; tuller@mit.edu

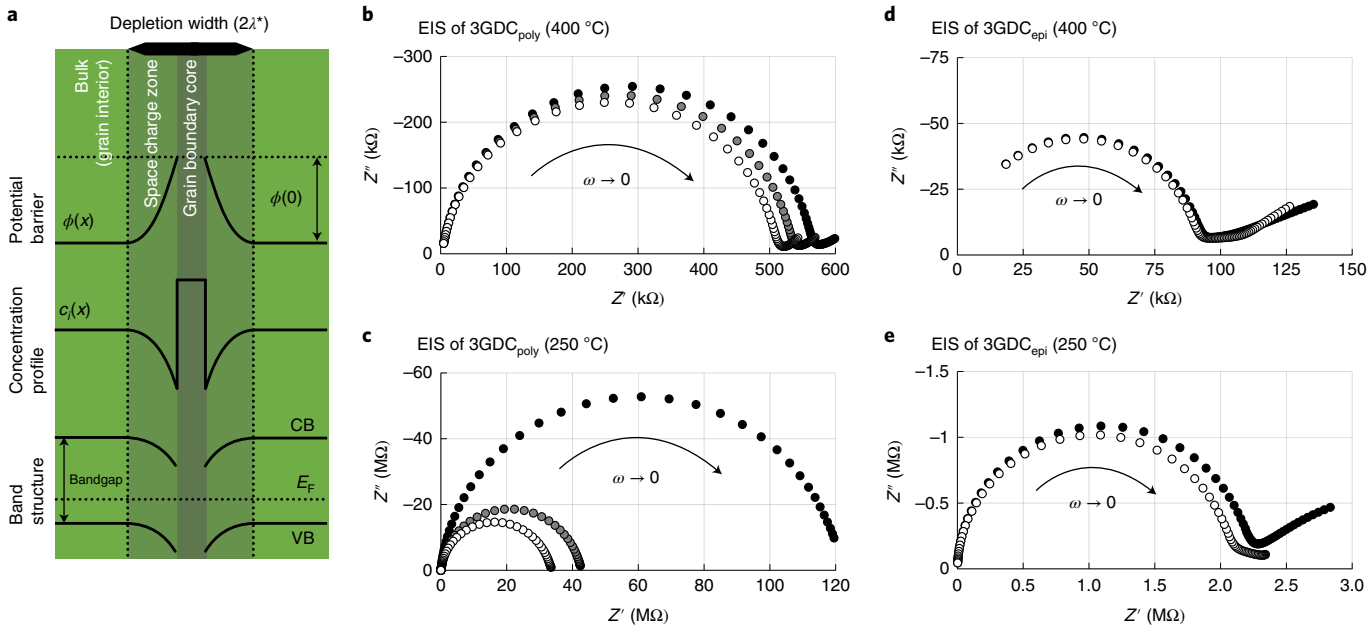

Fig. 1 | General grain boundary characteristics and the impact of UV illumination. a, Model representation of the general characteristics of the grain boundary core and the adjacent space charge zone for a polycrystalline electroceramic. $\phi(0)$ is the potential barrier that exists due to the net charge of the grain boundary core compared to the grain. In response to the potential barrier height, the defects in the adjacent grain redistribute according to the concentration profile $c_i(x)$ showing depletion in the space charge zone, over the extent of the depletion width (λ^*), and an accumulation in the grain boundary core of the species i, which are oxygen vacancies in the case of GDC. The band structure features the conduction band (CB), the valence band (VB) and the Fermi energy (E_F) lying below mid-gap in the dark. The band bending induced by the positive charges in the grain boundary core results in a downward bending of the CB and VB, resulting in a net electron accumulation and a net depletion of holes in the space charge regions. **b**–**e**, Impedance (Z, consisting of real, Z', and imaginary part, Z'') spectra measured on polycrystalline $3GDC_{poly}$ film (**b**,**c**) and epitaxially grown $3GDC_{epi}$ film (**d**,**e**) at 400 °C (**b**,**d**) and 250 °C (**c**,**e**), respectively, for different light intensities in synthetic air. Note substantial decreases in resistance with light in $3GDC_{poly}$ particularly at 250 °C. Also please note the different orders of magnitude of $Z(\omega)$ for grain boundary resistance (**b**,**c**) and bulk resistance (**d**,**e**). Black filled symbols represent measurements in the dark, while open symbols represent measurements under maximum illumination intensity generated by the 375 nm LED (detailed specifications can be found in the Methods). The intermediate curves (**b**,**c**), denoted by grey filled symbols, represent measurements at 25% of maximum illumination intensity. Impedance measurements on additional samples were performed to confirm the reproducibility of the effect. Examples include those subjected to variations in light intensity and wavelength (Supplementary Sections 6, 7 and 14).

intensity-modulated photocurrent spectroscopy (IMPS)[34,35] as a means of characterizing photo-stimulated conduction effects.

In essence, we have discovered an opto-ionic effect that mitigates the grain boundary potential barrier. This effect can be used to increase the total ionic conductivity of polycrystalline ceramics. It can also serve as a rapid diagnosis or characterization tool for investigating grain boundary resistance and the implications it has on device operation. Eventually, it could guide efforts towards more efficient and better performing electrolytes for fuel cells, electrolysers, solid-state batteries and other electrochemical energy conversion systems.

Photoelectrochemical measurements demonstrating and characterizing the opto-ionic effect

Polycrystalline and epitaxial 3GDC thin films with thicknesses of ~250 nm were prepared by pulsed laser deposition (referred to as $3GDC_{poly}$ and $3GDC_{epi}$, respectively, in the following). The details of the sample fabrication are provided in the Methods, and the microstructural and optical characterization can be found in Supplementary Sections 2–4. EIS spectra in Fig. 1 show measurements taken in the dark and under steady-state illumination at 375 nm for two different light intensity levels for both $3GDC_{poly}$ and $3GDC_{epi}$. The Methods has details on the measurement protocol. Additional measurements are shown in Supplementary Sections 6, 7 and 14. The bulk contribution of the 3GDC is not visible for the $3GDC_{poly}$ in Fig. 1b because it is shielded by the stray capacity that forms between the substrate and electrodes[32,33]. The main observed semicircle for $3GDC_{poly}$ is ascribed to the grain boundary contribution[21,36]. Its characteristic frequency f_{char} and time constant τ, $\tau = (2\pi f_{char})^{-1}$, depend mainly on the grain boundary resistance of the sample and the electrode geometry. Bode plots for the imaginary parts of the impedance measurements, indicating the characteristic frequencies, are shown in Supplementary Section 5. The voltage dependence of the grain boundary space charge contributions is shown and discussed in Supplementary Section 9 as well. As indicated in Fig. 1b, there is a moderate but systematic decrease in grain boundary resistance of $3GDC_{poly}$ at 400 °C with increasing light intensity. At 250 °C (Fig. 1c), the decrease for $3GDC_{poly}$ under the highest illumination intensity is more than 72% (from 118 MΩ to 33 MΩ) or inversely a ×3.6 increase in grain boundary conductance. At 25% of the highest illumination intensity, it decreases to 42 MΩ or by ~64%, representing a ×2.8 increase in grain boundary conductance. The Arrhenius plot in Fig. 2 reveals an activation energy of 1.124 ± 0.032 eV for measurements taken in the dark, in good agreement with the literature data[31]. By fitting the results with equation (17) in the Supplementary Information, we obtain an average space charge potential of 0.25 eV (Supplementary Section 1 for details).

The tail at the low-frequency end of each spectrum, usually attributed to the electrode resistance[36], was confirmed by examining its sensitivity to different gas atmospheres, that is, synthetic air versus pure Ar (Supplementary Section 8).

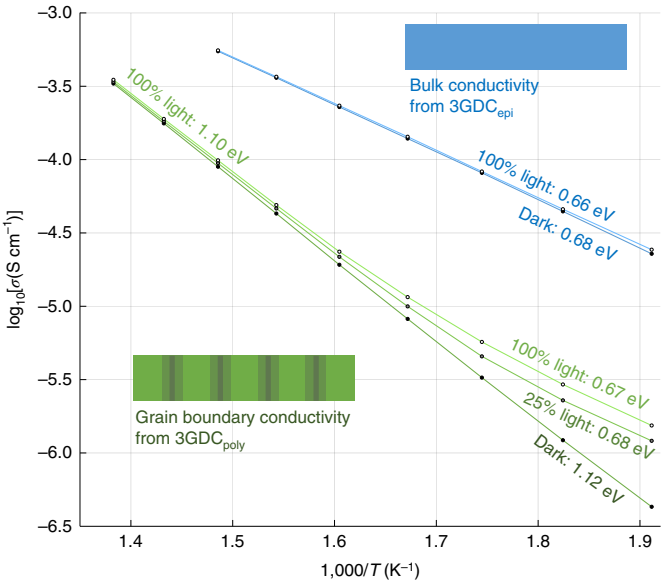

Fig. 2 | Temperature dependance of the opto-ionic effect. Arrhenius representation of the bulk conductivity (obtained from the epitaxial sample, $3GDC_{epi}$) and grain boundary conductivity (obtained from the polycrystalline sample, $3GDC_{poly}$) in the dark and under different levels of illumination; 100% light corresponds to 630 mW cm^{-2} of 375 nm light. The activation energy of ~0.67 eV for $3GDC_{poly}$ at the lowest temperatures under light was confirmed by additional measurements, which are shown in Extended Data Fig. 1, Supplementary Fig. 9 and Supplementary Table 1. Synthetic air was used for all measurements. σ, conductivity; T, temperature.

The EIS spectra measured on $3GDC_{epi}$, shown in Fig. 1d,e, exhibit orders-of-magnitude lower impedance than those measured for $3GDC_{poly}$ in Fig. 1b,c, as expected. The main semicircle is attributed to bulk ion transport. With an activation energy of 0.684 ± 0.009 eV and a conductivity of 8×10^{-5} S cm^{-1}, these characteristics are in good agreement with the literature data[31,36]. The magnitude of the main semicircle is insensitive to illumination at 375 nm at 400 °C and shows only a minor decrease at 250 °C. The low-frequency contribution to the impedance spectra, to the right of the semicircle, is attributed to the electrode resistance, which illumination appears to lower. While this is an interesting observation, because it is not the focus of this work and not relevant for bulk or grain boundary resistance, we do not explore this feature further.

The Arrhenius plot in Fig. 2 shows the conductivity values for both samples, obtained from the EIS measurements. It is apparent that neither the conductivity nor the activation energy change in any substantial manner for $3GDC_{epi}$ under illumination. By contrast, $3GDC_{poly}$ shows more than half an order of magnitude increase in grain boundary conductivity at 250 °C, corresponding to a resistance decrease by 72% when illuminated with maximum intensity (630 mW cm^{-2}). The impact of illumination is observed to become weaker with increasing temperature. While the magnitude of the resistance decrease at low temperatures shows little variation for different samples, other samples do show stronger sensitivity at high temperatures (Supplementary Sections 7 and 15). Importantly, we observe that the polycrystalline film's activation energy under illumination at the lower temperatures becomes essentially equal to that of the epitaxial film at the lowest temperatures.

Figure 3 shows single-frequency impedance transients (SFITs) at 300 °C, where the absolute magnitude of the impedance of the $3GDC_{poly}$ sample at 30 Hz is measured over time while repeatedly switching the light on and off. The duration of the on/off times is 50 s, respectively, with the SFIT measurement clearly demonstrating the repeatability of the opto-ionic effect.

Next, we report IMPS measurements made on $3GDC_{poly}$ at 400 to 460 °C and under 6 V applied d.c. bias voltage. IMPS represents the photocurrent response to light intensity modulation in the frequency domain. The IMPS spectra show the complex, frequency-dependent photocurrent admittance $Y_{pc}(\omega)$, reflecting how the photocurrent increases with light intensity with respect to the angular frequency ω. The photocurrent admittance $Y_{pc}(\omega)$ is normalized by the light intensity. $Y_{pc}(\omega)$ is directly related to the resistance decrease observed in Fig. 1 and reflects the dynamics and magnitude of this decrease. The IMPS spectra for $3GDC_{poly}$ are shown in Fig. 4a–d. For above-bandgap light (375 nm), the spectrum is composed of a large semicircle (corresponding to process P1) with a characteristic frequency of about 1 kHz, and a smaller semicircle (corresponding to process P2) (Fig. 4a) with a characteristic frequency between 0.3 Hz and 5 Hz (Fig. 4b). When illuminated with a 625 nm (below bandgap) light source, only a small low-frequency semicircle (P3) at 60 mHz appears (Fig. 4c,d). P1, in the spectra recorded with the 375 nm light source, represents the largest magnitude for all measurements. The activation energy calculated for the P1 time constant ($\tau=(2\pi f_{char})^{-1}$) is 0.7 eV (Fig. 4e).

As Fig. 4e shows, the smaller magnitude processes show much higher (P2, $E_a > 1.0$ eV) and much smaller (P3, $E_a \approx 0.3$ eV) activation energies than P1.

Modelling the opto-ionic effect

The EIS measurements shown in Fig. 1 demonstrate that there is a clear impact of optical illumination on the ionic grain boundary resistance in the $3GDC_{poly}$ sample. The diameter of the main semicircle, attributed to the grain boundary resistance $R_{gb,tot}$, decreased by 72% for a light intensity of 630 mW cm^{-2} at 250 °C, while for the $3GDC_{epi}$ sample, where the main semicircle is attributed to the bulk resistance $R_{bulk,tot}$, light had only a very minor impact.

In the following, we examine the expected effect of optical illumination on the space charge potential with the assistance of a model previously developed for silicon grain boundaries[28]. For a complete derivation of the model describing how photo-generated charge carriers can affect the grain boundary space charge potential, we refer the reader to papers by Bhatt et al. and Seager[28,37].

Here, we generalize the model to ionic conductors. The basic principles are summarized in Fig. 5. The physics controlling the phenomenon rely on the competition of the photo-generation rate G in the bulk of the material, the transport rate of the photo-generated electrons into the space charge region (J_e), the trapping rate of the photo-generated species into the grain boundary core energy traps (c), the transport of valence band holes to the grain boundary core as the band bending is decreased (J_h) and the recombination of the trapped electrons with the holes reaching the grain boundary core (J_r). Ultimately, the equilibrium between all quantities (G, J_e, c, J_h, J_r) is achieved when the electron trapping rate ($c\times J_e$) equals the hole recombination rate (J_r), which is assumed to be equal to J_h. The later phase of the transient process will depend on the slowest process, which is expected to be hole transport within the space charge zone.

As discussed in Supplementary Section 12, following the derivation by Seager, a governing equation describing the space charge potential at the grain boundary core with respect to extrinsic parameters such as the photo-generation rate G can be obtained. Assuming certain relevant material parameters listed in Supplementary Table 4 (Supplementary Section 12), which were either extracted from the literature or estimated from other material systems similar to 3GDC, we numerically simulate the impact of optical illumination on the specific grain boundary space charge potential. Supplementary Fig. 16 shows the obtained space charge potential as a function of light intensity in Gd-doped CeO_2 for different baseline space charge potentials, as extracted from the main governing model equation.

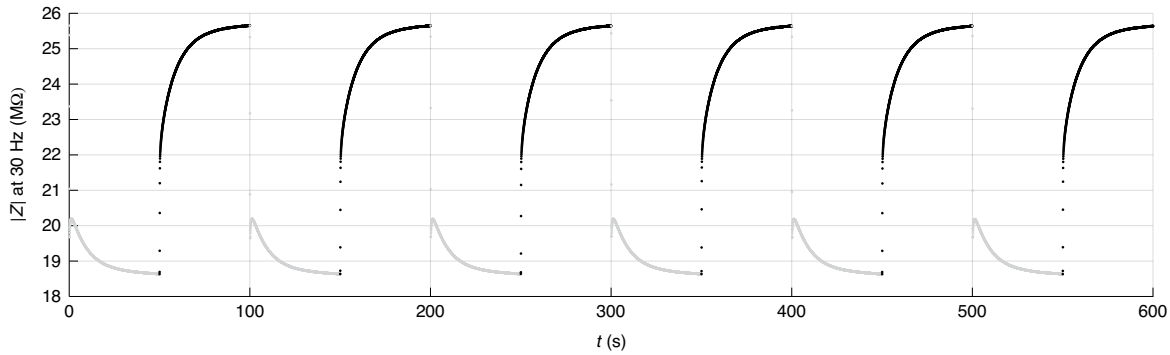

Fig. 3 | SFITs in light and dark phases. SFIT measurements on the $3GDC_{poly}$ sample during on/off illumination cycles with the 375 nm LED at 300 °C in synthetic air. The grey points indicate the light-on phases, while the black points indicate light-off phases. Measurement frequency is 30 Hz, filtered by a low-pass filter (filter frequency 3 Hz) and measured with a sampling rate of 38 ms. More details about the SFIT measurement can be found in Supplementary Section 10.

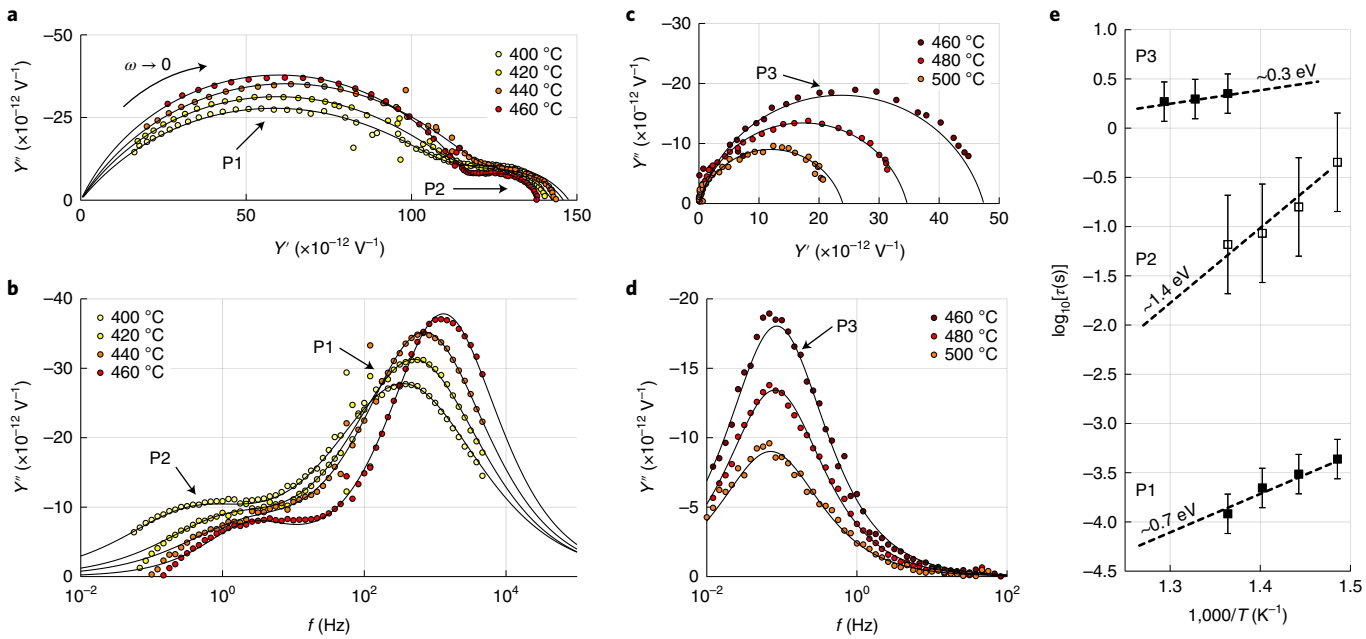

Fig. 4 | Frequency-dependent optical modulation of resistance response by IMPS. a–d, IMPS spectra measured on $3GDC_{poly}$ in synthetic air. Nyquist plots (**a** and **c**) of the photocurrent admittance (Y, consisting of real, Y', and imaginary part, Y'') and plots of the imaginary parts of $Y(\omega)$ as a function of frequency (**b** and **d**). Wavelengths of the light sources are 375 nm (**a** and **b**) and 625 nm (**c** and **d**). The points represent the measurement, and the solid lines are model fits using an empirical equivalent circuit model[35] after correcting for an inductive artefact caused by the measurement set-up. **e**, Arrhenius plots of the obtained time constants for the individual processes. The dashed lines are guides for the eye with the fitted activation energies indicated. The error bars represent confidence intervals obtained from the fitting procedure.

The model predicts that the grain boundary space charge potential can be substantially depressed by increasing the photo-generation rate. Consequently, mobile defects in the space zone will rearrange to respond to that change in space charge potential. As described in Supplementary Section 1, oxygen vacancies, which are the majority charge carriers at the temperatures being examined, will reflect the major change in concentration profile by reducing their level of depletion that is normally found under equilibrium in the space charge region in the dark—effectively shrinking its width. For the required readjustment of the space charge width, the actual distances that individual vacancies need to travel is on the same order of magnitude as the space charge width or less. Thus, for an ionic diffusivity of $10^{-8}\,cm^2\,s^{-1}$ to $10^{-10}\,cm^2\,s^{-1}$, and a diffusion distance of 1–7 nm, one expects vacancy redistribution to take on the order of milliseconds to seconds.

Looking at the activation energy obtained for the frequency of P1 from IMPS (~0.7 eV; Fig. 4e), it falls well within the range of activation energies associated with oxygen ion migration in GDC and matches well the measured value for the activation energy of 0.68 eV for ionic conduction in our epitaxial film. Moreover, assuming a diffusion distance x on the order of the space charge width (~1 nm), we can estimate the diffusivity controlling that process, which for a 1 kHz peak frequency would yield an observed diffusivity $D = x^2/2\tau \approx 10^{-12}\,cm^2\,s^{-1}$. This is very close to the expected magnitude of oxygen ion diffusivity in 3GDC ($D_O \approx 10^{-11}\,cm^2\,s^{-1}$) when considering the site fraction of oxygen vacancies (V) to oxy-

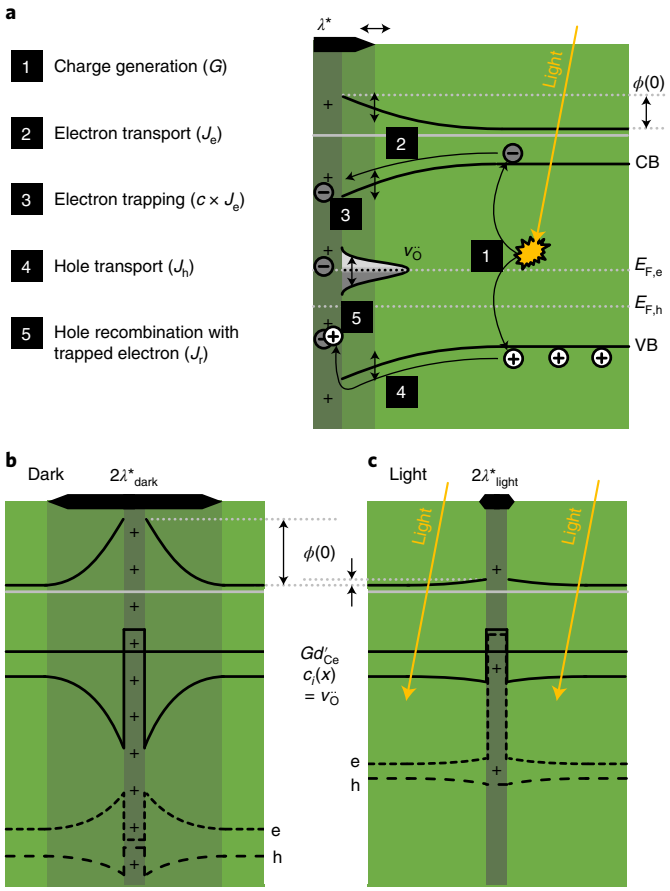

Fig. 5 | Suggested mechanism of the opto-ionic effect and the consequences for potential distribution and charge carrier concentrations. a, Individual steps responsible for the reversible decrease in the grain boundary potential barrier shown in combined schematics of potential (above the grey line) and charge carrier concentrations (below the grey line). The thin double arrows indicate the opposing consequences due to steps 3 (trapping of electrons) and 5 (recombination), respectively, for potential distribution, density of states (oxygen vacancies) in the grain boundary core and band bending. **b**,**c**, Grain boundary potential ϕ and the space charge width, as well as concentrations of Gd dopants on Ce sites (Gd'_{Ce}), doubly positively charged oxygen vacancies ($c_i(x) = v_{O^{\cdot\cdot}}$), holes (h) and electrons (e) in the dark (**b**) and under illumination (**c**). Panel **c** shows an extreme case of a nearly fully collapsed grain boundary potential barrier, for which the concentration of accumulated electrons in the grain boundary core nearly matches the concentration of oxygen vacancies under equilibrium (dark). Quasi-Fermi energies for electrons and holes ($E_{F,e}$, $E_{F,h}$), depletion width in the dark (λ^*_{dark}) and under light (λ^*_{light}).

gen ions (O) in the lattice $n_v = [V]/[O]$ (square brackets refer the concentration of the respective species) (ref. [38]) with $D_O \approx n_v D_v$ (Supplementary Section 1 explains the relation between oxygen ion diffusivity (D_O) and vacancy diffusivity (D_v)). As we expect slightly faster oxygen transport due to drift in the space charge region, the kinetics of oxygen migration match the measured peak frequency very well, and this is a strong indication that the initial resistance decrease is indeed dominated by the rearrangement of oxygen ions in the space charge region. Moreover, using a similar logic for the behaviour of P2, we find that for a peak frequency of 1 Hz, the observed diffusivity would be $D = x^2/2\tau \approx 10^{-14}\,cm^2\,s^{-1}$ with an activation energy >1.0 eV. While this would be considered too high a magnitude for cation diffusivity and too small a corresponding migration enthalpy[39,40], it does fall well in line with some experimentally reported diffusivities for holes in Gd-doped CeO_2 (ref. [41]). Given limited and inconsistent data for hole mobilities and even conduction mechanisms in the literature[41,42], we cannot confirm this assignment with certainty. Nevertheless, it is consistent with the model in which we propose that hole redistribution within the space charge region will ultimately control the steady-state recombination kinetics of trapped photo-generated electrons at the grain boundary core. On the other hand, the small-magnitude, low-frequency process P3 measured under illumination with the sub-bandgap 625 nm light source exhibits an activation energy that does not match those obtained with the 375 nm light, suggesting that it originates from a very different process that cannot be assigned to any of the known mobile species.

Ruling out other reasons for the opto-ionic effect

While these theoretical considerations have rationalized how above-bandgap illumination can reduce the grain boundary resistance in the $3GDC_{poly}$ film, we need to rule out other possible effects, such as photo-generated electronic conductivity and heating contributions. The fact that the $R_{bulk,tot}$ associated with bulk ion transport measured in the $3GDC_{epi}$ sample shows only a minor change due to illumination at 375 nm is the strongest evidence that the large measured decrease in resistance under illumination of the $3GDC_{poly}$ sample is not caused by heating or by electronic conductivity. If that were the case, the $3GDC_{epi}$ would react in a similar manner to light as $3GDC_{poly}$. The convergence of $R_{gb,tot}$ for higher bias voltages in Supplementary Fig. 14a is another strong indication that light-induced heating plays at best a very minor role, as heating would also decrease the resistance under a voltage bias. Furthermore, a higher bias should lead to a more efficient collection of photo-generated electronic carriers, which is not observed.

To further verify that heating is not contributing to the observed enhancements in ionic conductivity, we estimate the expected increase in temperature of the illuminated area by employing the thermal spreading resistance formula for the 3GDC thin films that assumes all the heat generated due to the light source is dissipated through the substrate. As detailed in Supplementary Section 13, the increase in temperature is expected to be less than 1 °C, even if all the incident irradiation power is converted directly into heat. We also applied Raman spectroscopy to measure the temperature increase of an illuminated spot by examining lattice expansion. Again, both the analysis of the Stokes F_{2g} stretching mode of O–Ce–O in the lattice, indicating no distortions in the oxygen vacancy sublattice, and thermometric measurements based on the temperature dependence of the Stokes/anti-Stokes relative intensity contributions point to a temperature increase of less than 1 °C.

Several other questions still require attention. First, referring to Fig. 2, why is the resistance of $3GDC_{poly}$ still an order of magnitude larger than that of $3GDC_{epi}$ at lower temperatures, even though the activation energy becomes essentially equal to that of oxygen migration in the bulk? In Supplementary Section 14, we provide a detailed explanation based on model constriction effects that originate from remaining grain boundary barriers, but with a conduction path free from grain boundary limitations. Also, the resistance decrease versus the logarithm of the light intensity reveals a nearly linear relationship beyond 10% of the maximum light intensity (Supplementary Section 7 and Supplementary Fig. 11c), which suggests that further decreases in resistance with increased light intensity are possible.

Second, why is the opto-ionic effect weaker at higher temperatures? While this can be explained by the constricted conduction path on the one hand, we additionally expect shorter recombination times of the photo-generated charge carriers at increased temperatures in the bulk (Supplementary Section 15). These shorter times will reduce the number of charge carriers that are eventually able

to reduce the space charge potential. This would be in line with a Shockley–Read–Hall recombination mechanism, which relates the carrier lifetime to the inverse of the thermal velocity.

Third, we need to consider what might be the source of the small resistance decrease seen in the $3GDC_{epi}$ sample under illumination. This decrease is notably smaller than that for the $3GDC_{poly}$ sample, and we suspect it to be related to a surface effect or space charge effects at the contacts. The substantial difference in absolute resistance change observed for the $3GDC_{poly}$ sample as compared to the $3GDC_{epi}$ sample (at 250 °C, $\Delta R_{gb,tot} = 85.1\,M\Omega$, $\Delta R_{bulk,tot} = 760\,k\Omega$; at 400 °C, $\Delta R_{gb,tot} = 53.7\,k\Omega$, $\Delta R_{bulk,tot} = 1.2\,k\Omega$) lets us conclude confidently that the discussed opto-ionic effect on the grain boundary resistance of the ionic conductor is the main reason for the resistance decrease of the $3GDC_{poly}$ sample under light.

From a broader perspective, comparing these results to existing strategies relying on chemical doping of the bulk lattice or the grain boundary core, optical illumination shows greater versatility in the sense that it can be turned on and off rapidly and controlled in magnitude and at will, if the technical challenge associated with integrating the light source and the limited penetration depth of the light are addressed. Also, it avoids common drawbacks that can be associated with doping such as the formation of insulating impurity phases, induced lattice phase transitions, changes in grain boundary chemistry and defect association leading to reduced bulk ionic migration.

Summary and outlook

Optical illumination above the bandgap of 3GDC polycrystalline ceramics has been demonstrated to increase ionic conductivity nearly fourfold at 250 °C, tied to a photo-induced reduction in the grain boundary space charge potential. Light-induced heating and electronic conductivity could be excluded as potential sources for the observed opto-ionic effect. By demonstrating that light predominantly enhances ionic rather than electronic conduction, the desired high ionic transference number of solid electrolytes is not compromised, which is important, for example, in the development of intermediate-temperature fuel cells. We believe this phenomenon is not restricted to the case of oxygen solid electrolytes and that it can be more widely applied to materials systems where space charge effects at grain boundaries impede ionic motion. If the concept can be adapted, for example, for lithium batteries, it could be used to boost battery performance by increasing charging rates. Likewise, its application as a diagnostic tool to investigate the impact of blocking grain boundaries on the formation of dendrites[43] could turn out to be a powerful complement. Furthermore, the idea that light at different intensities can gradually turn off different space charge potentials becomes a very interesting tool for studying the nature and distribution of grain boundaries in polycrystalline thin films in operando.

Moreover, the opto-ionic concept itself is not restricted to light-modulated grain boundary ionic conductivity but could be useful for many applications where ion migration, titration or controlled conduction is required, such as in memristors or displays. Given that these typically operate under near-ambient conditions, the impact of illumination can be expected to be much more dramatic. Further, light can be masked or focused, pointing to the potential for spatial control of ion transport.

Online content

Any methods, additional references, Nature Research reporting summaries, source data, extended data, supplementary information, acknowledgements, peer review information; details of author contributions and competing interests; and statements of data and code availability are available at https://doi.org/10.1038/s41563-021-01181-2.

Received: 17 April 2020; Accepted: 1 December 2021;
Published online: 13 January 2022

References

1. Kreuer, K. D. Proton conducting oxides. *Annu. Rev. Mater. Res.* **33**, 333–359 (2003).
2. Tuller, H. L. & Nowick, A. S. Doped ceria as a solid oxide electrolyte. *J. Electrochem. Soc.* **122**, 255–259 (1975).
3. Skinner, S. J. & Kilner, J. A. Oxygen ion conductors. *Mater. Today* **6**, 30–37 (2003).
4. Hu, Y.-S. Batteries: getting solid. *Nat. Energy* **1**, 16042 (2016).
5. Garbayo, I. et al. Glass-type polyamorphism in Li-garnet thin film solid state battery conductors. *Adv. Energy Mater.* **8**, 1702265 (2018).
6. Pfenninger, R., Struzik, M., Garbayo, I., Stilp, E. & Rupp, J. L. M. A low ride on processing temperature for fast lithium conduction in garnet solid-state battery films. *Nat. Energy* **4**, 475–483 (2019).
7. Whittingham, M. S. Lithium batteries and cathode materials. *Chem. Rev.* **104**, 4271–4301 (2004).
8. Pagani, F. et al. Epitaxial thin films as a model system for Li-ion conductivity in $Li_4Ti_5O_{12}$. *ACS Appl. Mater. Interfaces* **10**, 44494–44500 (2018).
9. Janek, J. & Zeier, W. G. A solid future for battery development. *Nat. Energy* **1**, 16141 (2016).
10. Brett, D. J. L., Atkinson, A., Brandon, N. P. & Skinner, S. J. Intermediate temperature solid oxide fuel cells. *Chem. Soc. Rev.* **37**, 1568–1578 (2008).
11. Adler, S. B. Factors governing oxygen reduction in solid oxide fuel cell cathodes. *Chem. Rev.* **104**, 4791–4843 (2004).
12. Gao, Z., Mogni, L. V., Miller, E. C., Railsback, J. G. & Barnett, S. A. A perspective on low-temperature solid oxide fuel cells. *Energy Environ. Sci.* **9**, 1602–1644 (2016).
13. Mai, A., Haanappel, V. A. C., Uhlenbruck, S., Tietz, F. & Stöver, D. Ferrite-based perovskites as cathode materials for anode-supported solid oxide fuel cells. Part I. Variation of composition. *Solid State Ion.* **176**, 1341–1350 (2005).
14. Takamura, H., Okumura, K., Koshino, Y., Kamegawa, A. & Okada, M. Oxygen permeation properties of ceria-ferrite-based composites. *J. Electroceram.* **13**, 613–618 (2004).
15. Meng, Y. et al. Review: recent progress in low-temperature proton-conducting ceramics. *J. Mater. Sci.* **54**, 9291–9312 (2019).
16. Knauth, P. Inorganic solid Li ion conductors: an overview. *Solid State Ion.* **180**, 911–916 (2009).
17. Kerman, K., Luntz, A., Viswanathan, V., Chiang, Y.-M. & Chen, Z. Review—practical challenges hindering the development of solid state Li ion batteries. *J. Electrochem. Soc.* **164**, A1731–A1744 (2017).
18. Rahaman, M. N. *Ceramic Processing and Sintering* 2nd edn (CRC Press, 2003).
19. Pergolesi, D. et al. High proton conduction in grain-boundary-free yttrium-doped barium zirconate films grown by pulsed laser deposition. *Nat. Mater.* **9**, 846–852 (2010).
20. Gregori, G., Merkle, R. & Maier, J. Ion conduction and redistribution at grain boundaries in oxide systems. *Prog. Mater. Sci.* **89**, 252–305 (2017).
21. Kim, S., Kim, S. K., Khodorov, S., Maier, J. & Lubomirsky, I. On determining the height of the potential barrier at grain boundaries in ion conducting oxide. *Phys. Chem. Chem. Phys.* **18**, 3023–3031 (2016).
22. Kim, S. & Maier, J. On the conductivity mechanism of nanocrystalline ceria. *J. Electrochem. Soc.* **149**, J73 (2002).
23. Wu, J. F. & Guo, X. Origin of the low grain boundary conductivity in lithium ion conducting perovskites: $Li_{3x}La_{0.67-x}TiO_3$. *Phys. Chem. Chem. Phys.* **19**, 5880–5887 (2017).
24. Ma, C. et al. Atomic-scale origin of the large grain-boundary resistance in perovskite Li-ion conducting solid electrolytes. *Energy Environ. Sci.* **7**, 1638–1642 (2014).
25. Aguesse, F., López Del Amo, J. M., Roddatis, V., Aguadero, A. & Kilner, J. A. Enhancement of the grain boundary conductivity in ceramic $Li_{0.34}La_{0.55}TiO_3$ electrolytes in a moisture-free processing environment. *Adv. Mater. Interfaces* **1**, 1300143 (2014).
26. Mei, A. et al. Role of amorphous boundary layer in enhancing ionic conductivity of lithium–lanthanum–titanate electrolyte. *Electrochim. Acta* **55**, 2958–2963 (2010).
27. García-Martín, S., Amador, U., Morata-Orrantia, A., Rodríguez-Carvajal, J. & Alario-Franco, M. Á. Structure, microstructure, composition and properties of lanthanum lithium titanates and some substituted analogues. *Z. fur Anorg. und Allg. Chem.* **635**, 2363–2373 (2009).
28. Joshi, D. P. & Bhatt, D. P. Theory of grain boundary recombination and carrier transport in polycrystalline silicon under optical illumination. *IEEE Trans. Electron Devices* **37**, 237–249 (1990).
29. Fergus, J. W. Electrolytes for solid oxide fuel cells. *J. Power Sources* **162**, 30–40 (2006).

30. Schmitt, R. et al. A review of defect structure and chemistry in ceria and its solid solutions. *Chem. Soc. Rev.* **49**, 554–592 (2020).
31. Avila-Paredes, H. J., Choi, K., Chen, C. T. & Kim, S. Dopant-concentration dependence of grain-boundary conductivity in ceria: a space-charge analysis. *J. Mater. Chem.* **19**, 4837–4842 (2009).
32. Göbel, M. C., Gregori, G., Guo, X. & Maier, J. Boundary effects on the electrical conductivity of pure and doped cerium oxide thin films. *Phys. Chem. Chem. Phys.* **12**, 14351–14361 (2010).
33. Gerstl, M. et al. The separation of grain and grain boundary impedance in thin yttria stabilized zirconia (YSZ) layers. *Solid State Ion.* **185**, 32–41 (2011).
34. Peter, L. M. Dynamic aspects of semiconductor photoelectrochemistry. *Chem. Rev.* **90**, 753–769 (1990).
35. Klotz, D., Ellis, D. S., Dotan, H. & Rothschild, A. Empirical *in operando* analysis of the charge carrier dynamics in hematite photoanodes by PEIS, IMPS and IMVS. *Phys. Chem. Chem. Phys.* **18**, 23438–23457 (2016).
36. Harrington, G. F. et al. The interplay and impact of strain and defect association on the conductivity of rare-earth substituted ceria. *Acta Mater.* **166**, 447–458 (2019).
37. Seager, C. H. Grain boundary recombination: theory and experiment in silicon. *J. Appl. Phys.* **52**, 3960–3968 (1981).
38. De Souza, R. A. Oxygen diffusion in $SrTiO_3$ and related perovskite oxides. *Adv. Funct. Mater.* **25**, 6326–6342 (2015).
39. Rockenhäuser, C. et al. Microstructure evolution and cation interdiffusion in thin Gd_2O_3 films on CeO_2 substrates. *J. Eur. Ceram. Soc.* **34**, 1235–1242 (2014).
40. Beschnitt, S., Zacherle, T. & De Souza, R. A. Computational study of cation diffusion in ceria. *J. Phys. Chem. C* **119**, 27307–27315 (2015).
41. Jacobsen, T., Chatzichristodoulou, C. & Mogensen, M. B. Fermi potential across working solid oxide cells with zirconia or ceria electrolytes. *ECS Trans.* **61**, 203–214 (2014).
42. Gopal, C. B. & Haile, S. M. An electrical conductivity relaxation study of oxygen transport in samarium doped ceria. *J. Mater. Chem. A* **2**, 2405–2417 (2014).
43. Dong, Y. & Chen, I. W. Oxygen potential transition in mixed conducting oxide electrolyte. *Acta Mater.* **156**, 399–410 (2018).

Methods

Sample preparation. The GDC powder used to prepare the pulsed laser deposition target was synthesized through a coprecipitation route described by Spiridigliozzi et al.[44]. A solution of gadolinium and cerium in stoichiometric proportion (3:97) was prepared by dissolving cerium nitrate ($Ce(NO_3)_3{\cdot}6H_2O$) and gadolinium nitrate ($Gd(NO_3)_3{\cdot}6H_2O$; Strem Chemicals; 99.99%) in distilled water to reach a concentration of 0.1 mol l^{-1}. The precipitation solution was prepared by dissolving ammonium carbonate in distilled water to reach a concentration of 0.5 mol l^{-1}. The amount of ammonium carbonate solution was calculated to have a molar excess of 2.5 as compared to the total amount of cations in the nitrate solution. The ammonium carbonate solution was quickly poured into the vigorously stirred nitrate solution to trigger precipitation. The resulting precipitate was filtrated and washed four times in distilled water in a Buchner filter connected to a vacuum pump and dried at 100 °C overnight, followed by calcination at 600 °C for 1 h to obtain the GDC powder crystallized in the fluorite structure. The powder was then pressed into a 30-mm-diameter disc with a uniaxial press (1 ton cm^{-2}) and sintered at 1,500 °C for 6 h, followed by cooling at 1 °C min^{-1} to limit crack formation, resulting in a pellet with 97% density.

Both polycrystalline and epitaxial samples were grown by pulsed laser deposition (Surface) using a KrF excimer laser with a 248 nm wavelength (Coherent). The polycrystalline sample was directly grown on single crystal MgO(001), while the epitaxial sample was grown on an additional double buffer layer system of $BaZrO_3$ and $SrTiO_3$ (5 nm each), following a previously established procedure[45]. After a base pressure of 7×10^{-6} mbar was reached, pure oxygen was continuously leaked into the pulsed laser deposition chamber, keeping the total pressure at 0.013 mbar during the film growth and cooling steps. During deposition, the substrate temperature was held at 650 °C (heating rate 10 °C min^{-1} and cooling rate 1 °C min^{-1}). The laser energy was set to 100 mJ, resulting in a power density of about 1 J cm^{-2}. Target-to-substrate distance was 7.5 cm. The resultant GDC films formed a continuous pinhole-free layer. After depositing the samples, they were annealed in a tubular furnace at 900 °C with 5 °C min^{-1} ramp rates for 5 h in air to ensure complete oxidation of the lattice. Inter-digitated Pt electrodes with ten pairs of 180-μm-wide fingers spaced by 120 μm were deposited by using a shadow mask and d.c. magnetron sputtering at 50 W and 10 mtorr Ar.

Characterization by X-ray diffraction, atomic force microscopy and UV–visible spectroscopy. X-ray diffraction was performed by a Bruker cobalt source D8 with a General Area Detector Diffraction System. This system uses a conventional 1.6 kW sealed tube cobalt anode. Incident-side optics include a variety of double-pinhole collimators and monocapillary devices, which are used to adjust the beam size, intensity and divergence. The beam diameter for this instrument can range from 0.05 to 0.8 mm depending on the choice of collimator. The goniometer is a Open Eulerian Cradle that allows for motorized Chi - χ (tilt), Phi - φ (rotation) and X–Y–Z translations within the plane of the sample alongside conventional $2\theta/\omega$ scans. The Vantec-2000 detector has a very wide dynamic range and a maximum frame resolution of 2,048 × 2,048 pixels. Two-dimensional detectors facilitate the study of grainy and textured materials because the detector captures a slice of the Ewald diffraction sphere instead of a single point.

Topography maps were obtained by atomic force microscopy on a commercial Cypher AFM from Asylum Research. Images were obtained in tapping mode using PointProbe Plus Non-Contact Tapping Mode, High Resonance Frequency, Reflex Coating (PPP-NCHR) highly doped silicon probes from Nanosensors with tip radius below 10 nm and a nominal resonance frequency of 330 kHz. The images were processed using open-source software Gwyddion.

For the UV–visible measurements, a dual-beam spectrophotometer, custom built in our laboratory, was used. The spectrophotometer enables in situ measurements of the total optical transmission in a UV–visible–near-infrared wavelength range (350–900 nm) with 2 nm wavelength resolution. During the measurements, a controlled oxygen partial pressure (pO_2) atmosphere was maintained in an optical quartz flow cell where the characterized thin-film sample was held with a bare substrate used in the reference cell. The flow cell was placed in a tube furnace with parallel sapphire windows, enabling measurements from room temperature up to 900 °C.

Photoelectrochemical measurements. All photoelectrochemical measurements were performed in a Linkam stage HS600 with a quartz window allowing for heating and illumination of the sample. The chamber was flooded with 50 sccm of synthetic air to ensure oxidizing conditions throughout the measurement procedure. LEDs served as light sources with emission wavelengths of 375 nm and 625 nm (Thorlabs), providing narrow-band light with photon energies of 3.30 eV and 1.98 eV, respectively. The light was collimated and concentrated through optical components supplied by Thorlabs. Calibration was performed with a National Institute of Standards and Technology (NIST) traceable photosensor PDA36A-EC (Thorlabs). The LEDs were controlled by a DC2200 LED Driver (Thorlabs). The photoelectrochemical set-up was supplied with the photoelectrochemical extension to the Solartron Modulab as described below. The sample itself is partly covered by the interdigitated electrodes (IDEs), and the area exposed to the light was about 0.38 cm^2 (spot with diameter $\varnothing = 7$ mm), accounting for 60% of the film area (8 × 8 mm^2). The light intensity has been measured with a Thorlabs PM160T power meter. These considerations result in the following values for the reported 100% light intensity for the UV LED: 375 nm wavelength, 630 mW cm^{-2} power density, 243 mW power (spot with $\varnothing = 7$ mm), 1.2×10^{18} photons cm^{-2} s^{-1} irradiation and 4.6×10^{17} photons s^{-1} irradiation (spot with $\varnothing = 7$ mm). The respective values for the red LED are as follows: 625 nm wavelength, 719 mW cm^{-2} power density, 277 mW power (spot with $\varnothing = 7$ mm), 2.3×10^{18} photons cm^{-2} s^{-1} irradiation and 8.7×10^{17} photons s^{-1} irradiation (spot with $\varnothing = 7$ mm).

EIS and SFITs. All EIS measurements were performed with a MFIA Impedance Analyzer (Zurich Instruments). A 100 mV amplitude was necessary to achieve a sufficient current response in the highly resistive samples. The frequency range was 5 Hz to 1 MHz. Before each frequency sweep, the impedance was monitored at 5 Hz by the time-domain Plotter tool to ensure the sample had reached a steady state. Each EIS measurement was repeated at least once.

SFITs were performed at 30 Hz with an amplitude of 300 mV. For the data acquisition, the Plotter tool was used with a sampling time of 38 ms applying a low-pass filter ($f = 3$ Hz).

IMPS. IMPS measurements were performed with a ModuLab XM Photoelectrochemical Test System (Solartron). A short introduction to IMPS can be found in Supplementary Section 11. The IMPS measurements were performed at a bias voltage of 6 V and a bias light intensity of 50% of the rating of the LED, as described above. Since a beam splitter is introduced between the light source and sample to measure the dynamic light intensity required for the calculation of the photocurrent admittance $Y(\omega)$, the actual light intensity at the surface of the sample was considerably lower during IMPS measurements. The amplitude of the light intensity excitation was 20% of the bias light intensity as a standard. The frequency range of the measurements was chosen to range from 50 mHz to 100 kHz. At high frequencies, the measurements featured strong inductive effects, probably due to the leads of the LED and detector and the small measured currents through the sample. The inductive effect was identified by a simple equivalent circuit model, and the measured spectra were corrected for that inductive contribution.

Data availability

Source data are provided with this paper. Source data for Figs. 1–4 and Supplementary Figs. 9–11 are available from the online data repository Figshare with identifier https://doi.org/10.6084/m9.figshare.c.5707109.v4. Remaining data that support the findings of this study are available from the corresponding authors upon reasonable request.

References

44. Spiridigliozzi, L. et al. Engineered co-precipitation chemistry with ammonium carbonate for scalable synthesis and sintering of improved $Sm_{0.2}Ce_{0.8}O_{1.90}$ and $Gd_{0.16}Pr_{0.04}Ce_{0.8}O_{1.90}$ electrolytes for IT-SOFC. *J. Ind. Eng. Chem.* **59**, 17–27 (2018).
45. Sanna, S. et al. Fabrication and electrochemical properties of epitaxial samarium-doped ceria films on $SrTiO_3$-buffered MgO substrates. *Adv. Funct. Mater.* **19**, 1713–1719 (2009).

Acknowledgements

We thank G. F. Harrington for the valuable input on sample preparation and characterization and K. May for help with the atomic force microscopy measurements. T.D. and H.L.T. acknowledge support for their research from the US Department of Energy, Basic Energy Sciences under award number DE-SC0002633 (Chemomechanics of Far-From-Equilibrium Interfaces). D.K. acknowledges support by the Japan Society for the Promotion of Science Core-to-Core Program, A. Advanced Research Networks: 'Solid Oxide Interfaces for Faster Ion Transport', as well as funding from the Kakenhi Grant-In-Aid for young scientists, grant numbers 18K13993 and 20K15028. D.K. and H.L.T. appreciate preliminary discussions with H. Matsumoto of Kyushu University and T. Lippert and D. Pergolesi of the Paul Scherrer Institute. J.L.M.R., J.C.G.-R. and T.D. acknowledge the Swiss National Science Foundation for grant number BSSGI0_155986/1, and Equinor for grant Agr no. 4502981450. This work made use of the Materials Research Science and Engineering Center Shared Experimental Facilities at the Massachusetts Institute of Technology, supported by the National Science Foundation under award number DMR-14-19807. A portion of this work was performed at the Center for Nanoscale Systems, a member of the National Nanotechnology Coordinated Infrastructure Network, which was supported by the National Science Foundation under National Science Foundation award no. 1541959.

Author contributions

H.L.T. conceived the concept; T.D. and D.K. performed all experiments except the atomic force microscopy and scanning electron microscopy experiments, which were performed by J.C.G.-R.; H.L.T. and J.L.M.R. supervised the work. The manuscript was

written by T.D., D.K., J.L.M.R. and H.L.T., and all authors contributed to discussions and editing.

Competing interests
The authors declare no conflict of interest.

Additional information
Extended data is available for this paper at https://doi.org/10.1038/s41563-021-01181-2.

Supplementary information The online version contains supplementary material available at https://doi.org/10.1038/s41563-021-01181-2.

Correspondence and requests for materials should be addressed to Thomas Defferriere, Dino Klotz or Harry L. Tuller.

Peer review information *Nature Materials* thanks Koji Amezawa and the other, anonymous, reviewer(s) for their contribution to the peer review of this work.

Reprints and permissions information is available at www.nature.com/reprints.

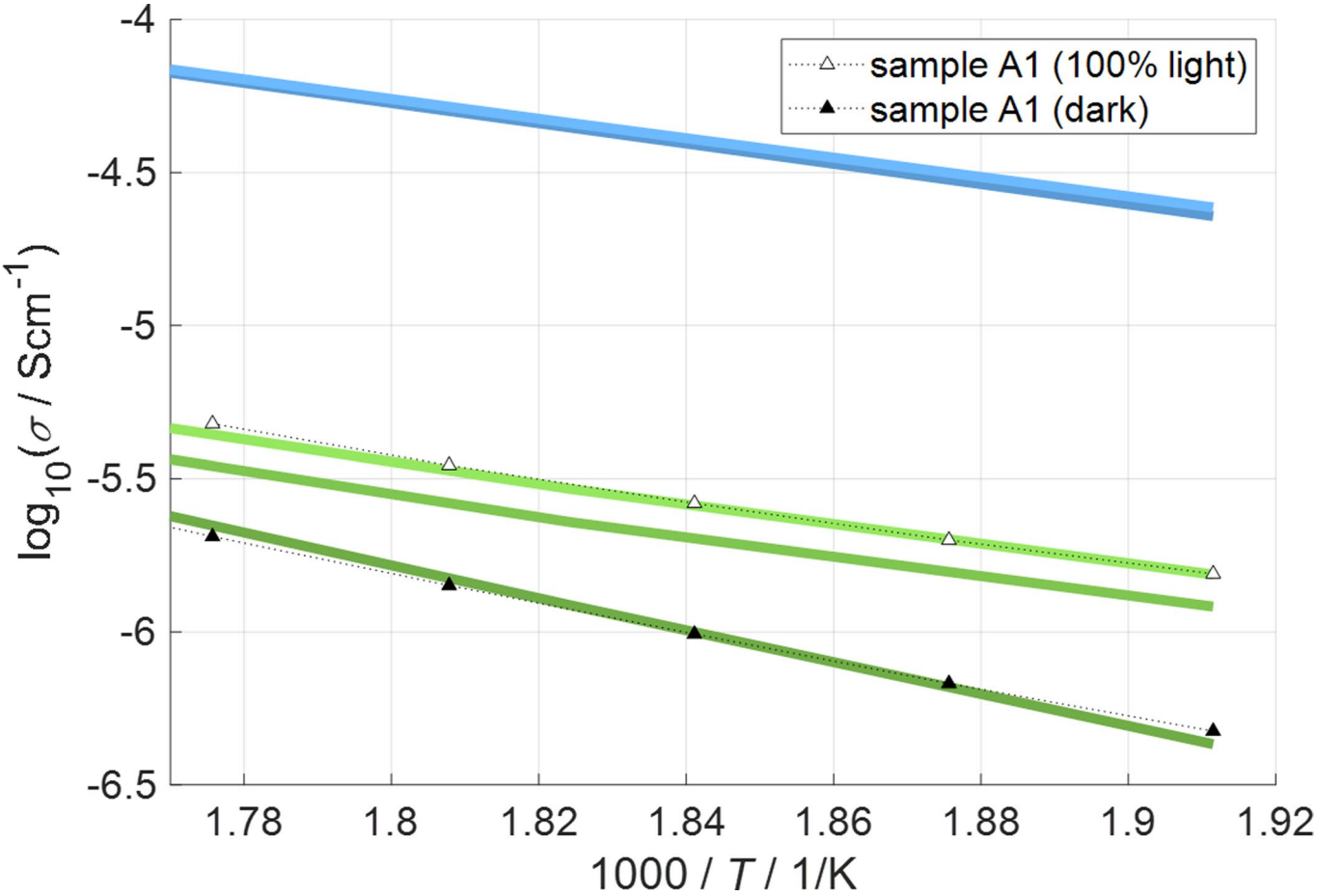

Extended Data Fig. 1 | Additional polycrystalline sample measured at low temperatures. Arrhenius plot of additional sample A1. As guide, the measurements of the epitaxial and polycrystalline samples from the main text are also plotted as full lines in the same color code as in the main text (same Figure appears as Supplementary Fig. S9).